Title

Cortical Synchrony and Information Flow during Transition from Wakefulness to Light Non-Rapid Eye Movement Sleep

Permalink

https://escholarship.org/uc/item/1w97w97q

Journal

Journal of Neuroscience, 43(48)

ISSN

0270-6474

Authors

Fan, Joline M

Kudo, Kiwamu

Verma, Parul

et al.

Publication Date

2023-11-29

DOI

10.1523/jneurosci.0197-23.2023

Peer reviewed

Systems/Circuits

Cortical Synchrony and Information Flow during Transition from Wakefulness to Light Non-Rapid Eye Movement Sleep

Joline M. Fan,[1] ●**Kiwamu Kudo,**[2,3] **Parul Verma,**[2] **Kamalini G. Ranasinghe,**[1] **Hirofumi Morise,**[2,3] **Anne M. Findlay,**[2] **Keith Vossel,**[1,5] **Heidi E. Kirsch,**[1,2] **Ashish Raj,**[2] **Andrew D. Krystal,**[4] and **Srikantan S. Nagarajan**[2]

[1]Department of Neurology, University of California–San Francisco, San Francisco, California 94143, [2]Department of Radiology and Biomedical Imaging, University of California–San Francisco, San Francisco, California 94143, [3]Medical Imaging Center, Ricoh Company, Ltd., Kanazawa, Japan 243-0460, [4]Department of Psychiatry, University of California–San Francisco, San Francisco, California 94143, and [5]Mary S. Easton Center for Alzheimer's Disease Research, Department of Neurology, David Geffen School of Medicine, University of California–Los Angeles, Los Angeles, California 90095

Sleep is a highly stereotyped phenomenon, requiring robust spatiotemporal coordination of neural activity. Understanding how the brain coordinates neural activity with sleep onset can provide insights into the physiological functions subserved by sleep and the pathologic phenomena associated with sleep onset. We quantified whole-brain network changes in synchrony and information flow during the transition from wakefulness to light non-rapid eye movement (NREM) sleep, using MEG imaging in a convenient sample of 14 healthy human participants (11 female; mean 63.4 years [SD 11.8 years]). We furthermore performed computational modeling to infer excitatory and inhibitory properties of local neural activity. The transition from wakefulness to light NREM was identified to be encoded in spatially and temporally specific patterns of long-range synchrony. Within the delta band, there was a global increase in connectivity from wakefulness to light NREM, which was highest in frontoparietal regions. Within the theta band, there was an increase in connectivity in fronto-parieto-occipital regions and a decrease in temporal regions from wakefulness to Stage 1 sleep. Patterns of information flow revealed that mesial frontal regions receive hierarchically organized inputs from broad cortical regions upon sleep onset, including direct inflow from occipital regions and indirect inflow via parieto-temporal regions within the delta frequency band. Finally, biophysical neural mass modeling demonstrated changes in the anterior-to-posterior distribution of cortical excitation-to-inhibition with increased excitation-to-inhibition model parameters in anterior regions in light NREM compared with wakefulness. Together, these findings uncover whole-brain corticocortical structure and the orchestration of local and long-range, frequency-specific cortical interactions in the sleep-wake transition.

Key words: functional connectivity; information flow; MEG; neural mass modeling; NREM; sleep

Significance Statement

Our work uncovers spatiotemporal cortical structure of neural synchrony and information flow upon the transition from wakefulness to light non-rapid eye movement sleep. Mesial frontal regions were identified to receive hierarchically organized inputs from broad cortical regions, including both direct inputs from occipital regions and indirect inputs via the parieto-temporal regions within the delta frequency range. Biophysical neural mass modeling revealed a spatially heterogeneous, anterior-posterior distribution of cortical excitation-to-inhibition. Our findings shed light on the orchestration of local and long-range cortical neural structure that is fundamental to sleep onset, and support an emerging view of cortically driven regulation of sleep homeostasis.

Introduction

The transition to sleep involves a set of neural processes that reliably promotes a behavioral state-change and sets the stage for essential functions of sleep. Classical lesion and stimulation-based studies have identified that the sleep-wake transition is modulated by distributed circuits originating in the brainstem and extending to the hypothalamus, thalamus, and basal forebrain (Brown et al., 2012; Saper and Fuller, 2017). Such bottom-up regulation of sleep and wake has led to a model whereby cortical structures are globally activated by subcortical structures during state transitions. More recent studies, however, have identified the presence of local cortical dynamics during sleep (Huber et al., 2004; Krueger and Tononi, 2012; Siclari and Tononi, 2017; Bernardi et al., 2018; Kringelbach and Deco, 2020) and furthermore have suggested that the neocortex may even play a top-down role in sleep-wake regulation (Thomas et al., 2020; Krone et al., 2021). To this end, we pose the questions: Is there a structured coordination between local and long-range cortical dynamics during the transition from wake to light non-rapid eye movement (NREM)? If so, what are putative mechanisms mediating the local cortical dynamics? The elucidation of coordinated local and long-range cortical structure may ultimately shed light on cortically based physiologic phenomena, such as emotional regulation (Palmer and Alfano, 2017), memory consolidation (Klinzing et al., 2019), and recovery (Hobson and Pace-Schott, 2002), and pathologic phenomena of sleep onset, such as state-dependent epileptic spiking (Herman et al., 2001) or insomnia.

For many decades, sleep electrophysiology has been characterized by recordings from a limited number of scalp electrodes, as traditionally used in polysomnography. Meanwhile, fMRI/PET (Horovitz et al., 2008, 2009; Larson-Prior et al., 2009) studies have provided key anatomical insights on whole-brain neural activation patterns of sleep. Large-scale network analyses primarily using fMRI have revealed widespread increases in corticocortical connectivity and decreases in thalamocortical connectivity with the transition from wakefulness to light NREM (Liu et al., 2010a; Spoormaker et al., 2010; Tagliazucchi and Laufs, 2014); deep NREM has been associated with widespread decreases in functional connectivity (FC) and partial restoration of thalamocortical connectivity (Spoormaker et al., 2010; Tagliazucchi and Laufs, 2014). The diffuse increase in corticocortical FC from wakefulness to light NREM has been hypothesized to lead to reduced information integration, underpinning the loss of consciousness with sleep (Spoormaker et al., 2010, 2011). While fMRI/PET offer key insights on the relative activation of neuroanatomical sites with the transition to sleep, these imaging modalities are limited by low temporal resolution and their indirect nature of probing neural activity (e.g., fMRI measures blood flow and PET measures neural metabolic rate).

Complementing prior fMRI methods, several key MEG/EEG (De Gennaro et al., 2001, 2005; Ioannides et al., 2017) studies have elucidated frequency-specific patterns with sleep onset, including the robust increase in low-frequency oscillations in midline anterior brain regions, which later propagate posteriorly (De Gennaro et al., 2005). The increased corticocortical connectivity with sleep onset has been furthermore observed across multiple frequency bands using band-limited power correlations of MEG/EEG sensor time series (Liu et al., 2010b). To date, however, MEG/high-density EEG studies have been limited by the lack of a comprehensive assessment of simultaneous local and long-range neuronal synchrony and information flow with the transition from wakefulness to sleep. In addition, amidst findings of global changes in FC, distinct long-range cortical interactions have not previously been observed, which may reflect prior methodological limitations, including the following: limited measures of connectivity due to the lack of source reconstruction (Liu et al., 2010b); temporal blurring due to the lack of simultaneous EEG for sleep-scoring in MEG studies; and correlational connectivity methods that may introduce effects of volume conduction or other sources of spurious connectivity.

The cortical network electrophysiology across sleep-wake states not only dictates behavior, but also reflects the underlying homeostatic process (Tononi and Cirelli, 2006; Vyazovskiy et al., 2009). Sleep homeostasis has been measured using a variety of EEG indicators, including spectral power, estimated excitation-to-inhibition ratios, global synchrony, amplitudes of evoked responses, among others. Estimates of the excitatory-to-inhibitory balance, for example, have been demonstrated to increase with prolonged wakefulness and decrease with sleep, as well as fluctuate with other factors, such as circadian rhythm and medications (Meisel et al., 2015; Ly et al., 2016). Prior literature has provided evidence that the excitatory-to-inhibitory balance has sleep-state specificity, including increasing in NREM and decreasing in REM, as measured in humans by magnetic resonance spectroscopy (MRS) (Tamaki et al., 2020). Other studies suggest that the excitatory-to-inhibitory balance of deep NREM or slow-wave sleep may be distinct from light NREM and reduced compared with wakefulness (Niethard et al., 2016). The extent to which excitatory-to-inhibitory changes occur as a function of sleep-wake states remains an open question (Niethard et al., 2016), in part limited by the challenges of directly measuring excitation and inhibition in sleeping humans. Thus, computational methods based on electrophysiology have the potential to further elucidate such underlying mechanisms (Lombardi et al., 2017; Sukenik et al., 2021; Verma et al., 2022).

In this study, we analyzed data from a convenient sample of older adults to identify local and long-range cortical structure that underlie global state transitions from wakefulness to light NREM. We note that we evaluate a convenient sample of healthy adults who are older in age (mean age, 63.4 years [SD 11.8 years]). While quantitative age-related differences in network connectivity have been shown within sleep-wake states (Ujma et al., 2019; Bouchard et al., 2020, 2021), the overall patterns of FC also share significant similarities across age when comparing between sleep-wake states (Daneault et al., 2021). To this extent, we aim to provide a comprehensive assessment of simultaneous local and long-range neural synchrony and information flow across sleep-wake in a manner that has not previously been performed in the literature, while acknowledging that this study was performed in a convenient sample of older individuals.

Specifically, we pursued three aims: (1) to determine which cortical areas are preferentially activated by local synchronization during sleep onset using MEG imaging; (2) to simultaneously determine what cortical regions facilitate long-range synchronization upon the transition to sleep; and (3) to infer mechanisms underlying the observed network physiology using biophysical models. We hypothesized that there are frequency-specific, spatial patterns of corticocortical synchronization and information flow upon the transition from wakefulness to NREM. Furthermore, we hypothesized that spatially specific cortical patterns of neural synchronization reflect spatially heterogeneous excitatory-to-inhibitory activity during light NREM. To test these hypotheses, we leveraged the high spatiotemporal sensitivity of MEG imaging combined with simultaneous surface EEG to quantify spatiotemporal patterns of

local and long-range neural synchrony and information flow upon sleep onset in a cohort of healthy individuals.

Materials and Methods

Study cohort. MEG and simultaneously obtained scalp EEG data were obtained from a convenient sample of 14 healthy older individuals (age, mean 63.4 years [SD 11.8 years]; gender, female 11 of 14 [78.6%]). All participants were evaluated for any existing neurologic disorders by history and underwent a screening neurologic examination. While we recognize that older adults are known to have more variable sleep compared with younger adults (see limitations) (Mander et al., 2017; Li et al., 2018), the effects of aging are outside of the scope of this study, and all findings are reported based on group statistics. Exclusion criteria for this healthy cohort included any neurologic disorders by history or abnormal neurologic findings by examination. In addition, exclusion criteria included the use of any chronic or acute neuroactive medications, including neuroleptics, benzodiazepines, selective serotonin reuptake inhibitors/selective serotonin-norepinephrine reuptake inhibitors, or sedatives. Inclusion criteria included achieving at least an aggregate of 60 s within each sleep-wake state (W, Stage 1 [N1], and Stage 2 [N2], segmented into 15 s epochs, see below) during the EEG/MEG study. In all subjects, the use of these data for research was approved by the University of California San Francisco Institutional Review Board, and all subjects provided written informed consent prior to data collection.

Experimental design, data acquisition, and preprocessing. MEG scans were obtained using a whole-head biomagnetometer system (275 axial gradiometers; MISL), acquired in the supine position. MEG and simultaneous EEG data were obtained for a period of 50-70 min, recorded at a sampling rate of 600 Hz. Before the start of the recording, subjects were instructed to close their eyes and attempt to sleep. Subjects did not engage in any tasks during the recording. Raw EEG/MEG traces were chunked into 15 s epochs. Each epoch was visually inspected and rejected if there was presence of movement artifacts. In a subset of subjects with metallic artifacts from noncranial implants, a dual signal subspace projection algorithm was used for denoising (Cai et al., 2019). Epochs were scored into the appropriate sleep states based on scalp EEG criteria and using two-person validation according to the American Academy of Sleep Medicine criteria. The 15 s epochs of MEG data were then concatenated together to achieve at minimum, a 60 second time series representing each behavioral state. A maximum of the first eight artifact-free epochs (e.g., 120 s) were utilized in this analysis. Prior work demonstrated that 60 s of resting wake state is an adequate duration to reliably achieve stationarity for MEG time series analyses (Guggisberg et al., 2008).

Atlas-based source reconstruction was performed at the subject level to generate 14,125 isotropic voxels (each 5 mm in width) across a template MRI brain. Using individual MRIs and the nasion and tragus locations, the generated voxels were then warped onto each subject's brain. Magnetic lead-field vectors were computed for each voxel using a single-shell model approximation (Nolte, 2003) and indexed into the 210 cortical parcellations, defined by the Brainnetome atlas (Fan et al., 2016). We then used an array-gain scalar beamformer (Sekihara et al., 2004) applied to each 15 s sensor-based time series to obtain voxel-level time series. During the beamforming process, we normalized lead-field vectors to avoid artifact from the center-of-the-head. We then solved a generalized eigenvalue problem to determine the optimum source orientation (Sekihara and Nagarajan, 2008). Beamformer weights were computed in the time domain, and the sample covariance matrix of the sensors was computed from the sensor time series data. Truncated singular value decomposition techniques were used to invert the sensor covariance matrix with a truncation threshold of 10^{-6} × maximum singular value. The time series for each Brainnetome atlas-based cortical parcellation or ROI was subsequently determined by performing principal components analysis across the voxels level time series of each region and assigning the first principal component to each parcellation. Preprocessing and source reconstruction were performed using custom MATLAB scripts (version R2019a) integrated into the Fieldtrip toolbox (Oostenveld et al., 2011).

Data analysis and neural mass model (NMM). Time series data were bandpass filtered into the following frequency bands: delta (1-4 Hz), theta (4-8 Hz), alpha (8-12 Hz), sigma (12-15 Hz), and beta (15-30 Hz). Local neural synchrony was quantified by the normalized spectral power of the canonical frequency bands within a given ROI. Normalized spectral power was determined by dividing the power spectra by the total power.

Long-range synchrony was computed using imaginary coherence, an established spectral coherence measure of neural synchrony that is robust to volume conduction effects (Sanchez Bornot et al., 2018). Imaginary coherence was computed for all pairwise cortical parcellations. To evaluate the spatial patterns of connectivity (see regional-level statistics methods below), long-range synchrony associated with each cortical parcellation was computed by averaging all imaginary coherence values associated with each ROI (i.e., averaging the pairwise imaginary coherence matrix along one axis). The global mean of long-range synchrony was computed as the estimated mean across of all regions (see global-level statistics methods). We note that imaginary coherence is a shrinkage estimator of true synchrony that includes both real and imaginary components of coherence. Although near-zero lag can be observed in large-scale oscillatory networks (Rajagovindan and Ding, 2008; Viriyopase et al., 2012), imaginary coherence is favored given the concern for additional nonbiological synchrony that may be captured in zero-lag synchrony.

To capture information flow characteristics, phase transfer entropy (PTE) was first computed to assess the pairwise directional interactions between ROI time courses (Lobier et al., 2014). The strength of the directionality of information flow was then computed using a directionality index (i.e., directional PTE [dPTE]), a connectivity measure for quantifying information flow directionality that is robust to noise and linear signal mixing (Hillebrand et al., 2016; Kudo et al., 2021). The methods in which dPTE were computed are detailed in Kudo et al. (2021). Specifically, dPTE captures the relative strength of the directionality of information flow, as computed below (i.e., from ROI i to j) whereby the PTE represented below is normalized and dPTE is bound by [–1, 1]:

$$dPTE_{i \to j} = \frac{PTE_{i \to j}(f) - PTE_{j \to i}(f)}{PTE_{i \to j}(f) + PTE_{j \to i}(f)} \tag{1}$$

The dPTE matrices are represented by an asymmetric matrix. Data analysis was performed using the FieldTrip Matlab Toolbox (Oostenveld et al., 2011) and custom-made MATLAB code (version R2019a).

In addition, we utilized a linear, deterministic NMM (David and Friston, 2003; Moran et al., 2013; Raj et al., 2020; Verma et al., 2022) to gain mechanistic insights on the relative balance of excitatory and inhibitory inputs based on the observed spectra. This NMM captures the local neural activity, as measured by the power spectral density (PSD) across each ROI and sleep-wake state. In this implementation of the NMM, whole-brain dynamics are deterministically modeled in closed form within the Fourier domain, using a canonical rate model that considers local cortical neural activity (Raj et al., 2020; Verma et al., 2022). Specifically, we modeled a local signal as the summation of excitatory signals, $x_e(t)$, and inhibitory signals, $x_i(t)$, for every ROI, based on the Brainnetome cortical parcellation (Fan et al., 2016). We modeled the evolution of $x_e(t)$ and $x_i(t)$ by the following processes: (1) the decay of the individual signals with fixed neural gain parameters (g_{ee}, g_{ii}), (2) incoming signals from coupled excitatory and inhibitory populations (i.e., feedback interactions), and (3) a Gaussian white noise source (Eqs. 2, 3). The decay and the feedback interactions are regulated by characteristic time constants (τ_e, τ_i) to account for the rate of local circuit delays. With $f_e(t)$ and $f_i(t)$ as the ensemble-average neural response function, the signals $x_e(t)$ and $x_i(t)$ are modeled as the following:

$$\frac{dx_e(t)}{dt} = -\frac{f_e(t)}{\tau_e} \star \left(g_{ee} x_e(t) - g_{ei} f_i(t) \star x_i(t) \right) + p(t) \tag{2}$$

$$\frac{dx_i(t)}{dt} = -\frac{f_i(t)}{\tau_i} \star \left(g_{ii} x_i(t) + g_{ei} f_e(t) \star x_e(t) \right) + p(t) \tag{3}$$

Here, the input white noise term represented by $p(t)$; the neural gains are g_{ee}, g_{ii}, g_{ei}; the characteristic time constants are given by τ_e, τ_i; and $\star$
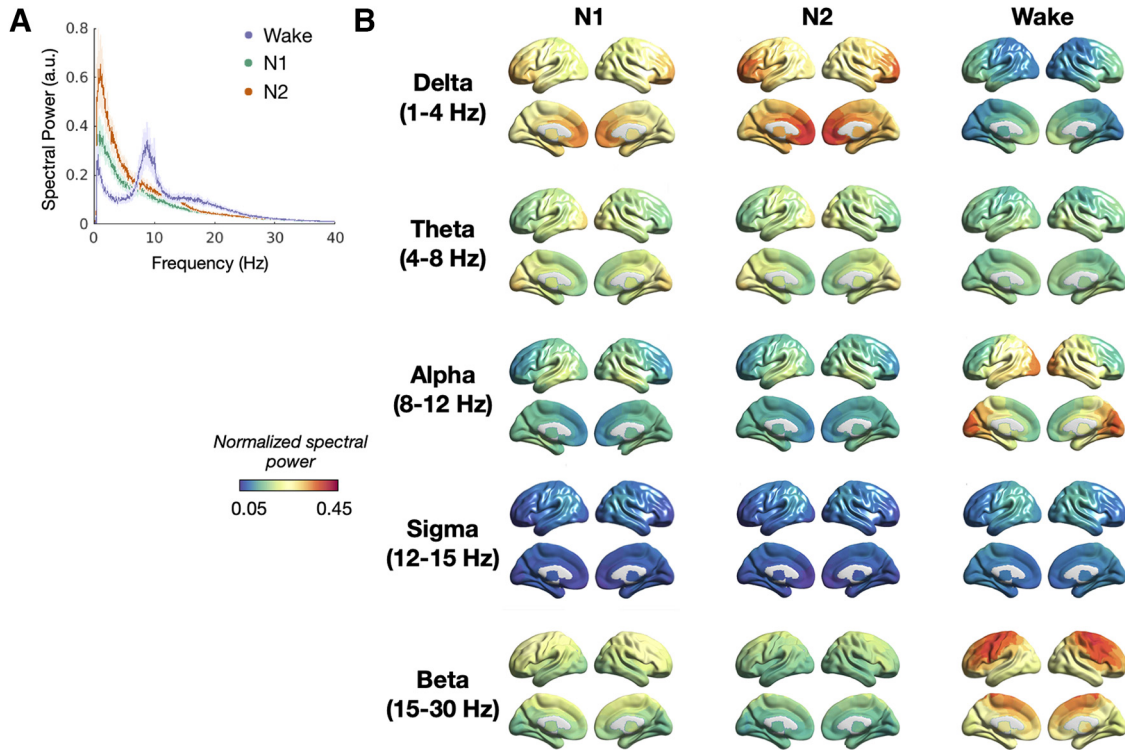
Figure 1. Spatial maps of local synchrony across sleep-wake states. **A**, Mean local synchrony, as measured by normalized spectral power, averaged across regions and participants in wake (purple), N1 (green), and N2 (orange). Light shading represents the SE across participants. **B**, Spatial maps of mean regional local synchrony across sleep-wake states.

stands for convolution. For optimization, g_{ei} was fixed at 1. The ensemble-average neural response function, $f_e(t)$ and $f_i(t)$, are assumed to be gamma-shaped (see Raj et al., 2020b, their Fig. 1b) and modeled as the following:

$$f_e(t) = \frac{t}{\tau_e^2} e^{\frac{-t}{\tau_e}} \quad (4)$$

$$f_i(t) = \frac{t}{\tau_i^2} e^{\frac{-t}{\tau_i}} \quad (5)$$

We assume that the signals $x_e(t)$ and $x_i(t)$ are presynaptic, and we incorporate the neural response functions ($f_e(t)$ and $f_i(t)$) to model the postsynaptic signals. Thus, the neural response functions are designed to represent both synaptic membrane capacitance and the distribution of dendritic/axonal delays introduced by the arborization. The key idea is that a neural signal cannot influence another population unless it passes through the neural response function. Similarly, the self-decay process of a neural element can only influence itself through the self-impulse response. This model is further described in Verma et al. (2023), Raj et al. (2020b), and Ranasinghe et al. (2022).

By taking the Fourier transform of Equations 1 and 2, $x_e(t)$ and $x_i(t)$ are then transformed into the Fourier domain and are expressed by $X_e(\omega)$ and $X_i(\omega)$, respectively, in which ω is the frequency:

$$j\omega X_e(\omega) = -\frac{F_e(\omega)}{\tau_e}(g_{ee}X_e(\omega) - g_{ei}F_i(\omega)X_i(\omega)) + P(\omega) \quad (6)$$

$$j\omega X_i(\omega) = -\frac{F_i(\omega)}{\tau_i}(g_{ii}X_i(\omega) + g_{ei}F_e(\omega)X_e(\omega)) + P(\omega) \quad (7)$$

Where j is the imaginary unit. Similarly, $P(\omega)$ represents the Fourier transform of $p(t)$, and $F_e(\omega)$ and $F_i(\omega)$ represent the Fourier transform of $f_e(t)$ and $f_i(t)$ and are expressed by the following:

$$F_e(\omega) = \frac{\frac{1}{\tau_e^2}}{\left(j\omega + \frac{1}{\tau_e}\right)^2} \quad (8)$$

$$F_i(\omega) = \frac{\frac{1}{\tau_i^2}}{\left(j\omega + \frac{1}{\tau_i}\right)^2} \quad (9)$$

Thus, the closed form solution of $X_e(\omega)$ and $X_i(\omega)$ is as follows:

$$X_e(\omega) = \frac{\left(1 + \frac{\frac{g_{ei}}{\tau_e}F_e(\omega)F_i(\omega)}{j\omega + \frac{g_{ii}}{\tau_i}F_i(\omega)}\right)P(\omega)}{j\omega + \frac{g_{ee}}{\tau_e}F_e(\omega) + \frac{(g_{ei}F_e(\omega)F_i(\omega))^2}{\tau_e\tau_i\left(j\omega + \frac{g_{ii}}{\tau_i}F_i(\omega)\right)}} \quad (10)$$

$$X_i(\omega) = \frac{\left(1 - \frac{\frac{g_{ei}}{\tau_i}F_e(\omega)F_i(\omega)}{j\omega + \frac{g_{ee}}{\tau_e}F_e(\omega)}\right)P(\omega)}{j\omega + \frac{g_{ii}}{\tau_i}F_i(\omega) + \frac{(g_{ei}F_e(\omega)F_i(\omega))^2}{\tau_e\tau_i\left(j\omega + \frac{g_{ee}}{\tau_e}F_e(\omega)\right)}} \quad (11)$$

The simulated spectra, $X(\omega)$, is comprised of the excitatory and inhibitory components summed together, for example, $X_e(\omega) + X_i(\omega)$. Using the transfer functions, $H_e(\omega)$ and $H_i(\omega)$, and $P(\omega)$ as the driving function, $X_e(\omega)$ and $X_i(\omega)$ can be re-expressed as $H_e(\omega)P(\omega)$ and $H_i(\omega)P(\omega)$, and thus, $X(\omega) = (H_e(\omega) + H_i(\omega))P(\omega)$. From here, the PSD is represented

by $\mathbb{E}(|X(\omega)|^2)$. Recall that $P(\omega)$ represents Gaussian noise and thus has a flat power spectrum. Therefore, $\mathbb{E}(|X(\omega)|^2) \propto |H_e(\omega) + H_i(\omega)|^2$, which is subsequently converted to dB scale by log-transformation: $10log_{10}(|H_e(\omega) + H_i(\omega)|^2)$.

For each ROI, g_{ee}, g_{ii}, τ_e, and τ_i were estimated. The spectra was modeled across frequencies 1-30 Hz, and the fit of the model was determined by calculating the mean squared error (MSE) between the simulated model PSD and the observed, source-localized MEG PSD in dB (with MEG dB spectra scaled by 2.5 to match the modeled spectra magnitude) across all frequencies. The minimization of the MSE for parameter optimization was then performed using the basin hopping global optimization algorithm in Python (Wales and Doye, 1997). The model parameter initialization value, upper-boundary, and lower-boundary were specified as 17, 5, and 30 ms, respectively, for τ_e, and τ_i; and 5, 0.1, and 10, respectively, for g_{ee} and g_{ii}. In addition, hyperparameters, including the number of iterations, step size, and temperature, were 2000, 4, and 0.1, respectively. If boundary values were hit during the parameter optimization, the step size was augmented to 6 for that specific ROI. The parameters leading to the lower MSE were then selected. This optimization procedure was performed for each Brainnetome topographical cortical parcellation for each subject and sleep-wake state. Model parameters whose fits were poor, defined by MSE >2 SDs above the mean MSE, were excluded from the analysis.

Statistical analysis. For all statistical comparisons, the 210 topographical cortical parcellations of the Brainnetome atlas were configured to 40 regions (modules), specified in Brainnetome atlas (Fan et al., 2016). The regional representations give rise to 820 functional connections, which include the averaged measure within each region.

In order to evaluate both sleep-wake state effects, we first performed "global" level statistics for each metric (e.g., connectivity, information flow, and model parameters). Specifically, we estimated the global mean of spectral power, imaginary coherence, and model parameters as a function of state, region, and subject using a linear mixed-effects model, for example, lm(imaginary_coherence ~ subject + region + state) or lm(XeXi ~ subject + region + state). We then ran a one-way ANOVA model with state as a factor. We report the estimated least-square means (LS-means; df 1675) and 95% CIs for each sleep-wake state. Pairwise contrasts to compare across sleep-wake states were adjusted for multiple comparisons across state using the Tukey–Kramer test. Statistical tests were performed in MATLAB (version R2019a) and R version 3.6.3.

We subsequently evaluated regional-level statistics (i.e., assessing connectivity, information flow, and model parameters within individual regions or pairs of regions) for the comparison across sleep-wake states. Here, we quantified the differences in regional-regional connectivity (i.e., region pairs) and information flow using a two-tailed, paired t tests to compare across sleep-wake states (i.e., between N1-N2, N1-W, N2-W). Topographical cortical parcellation pairs within each region pair were used as repeated measures. *Post hoc* corrections were performed to account for multiple comparison testing across all state and region pairs with a 5% false discovery rate (FDR). To compute differences in excitation-to-inhibition model parameters for each region, a two-tailed, paired t test was again performed across sleep-wake state comparisons. Topographical cortical parcellations within each region were used as repeated measures, and a *post hoc* correction was performed to account for multiple comparison testing (FDR 5%) across all state pairs and regions. To create spatial maps, regional measures (e.g., connectivity measures, model parameters, and thresholded T scores) were visualized on the brain using BrainNet Viewer (Xia et al., 2013).

To assess the relationship between mean regional local and long-range synchrony, regional spectral power and imaginary coherence were averaged across patients to represent the mean spectral power and imaginary coherence values for each region. The Pearson's correlation coefficient was then computed across all regions (i.e., each point represents one of 40 modules) within and across sleep-wake states.

Data availability. Anonymized summary data and relevant code will be made available for noncommercial research purposes upon request.

Results

Local neural synchrony across sleep states

Normalized spectral power, interpreted as local neural synchrony (Buzsáki and Watson, 2012; Buzsáki et al., 2012), was averaged across all regions and revealed an expected alpha peak during wakefulness and a shift toward delta frequencies with the transition from wakefulness to N1 and N2 (Fig. 1A). The source reconstructions of the mean normalized spectral power demonstrated an increase in delta power predominantly over the bilateral prefrontal cortices (Fig. 1B). The anterior-posterior gradient in the alpha frequency band, as well as the elevated beta power over the central regions, attenuated with the transition from wakefulness to light NREM (Fig. 1B). The spectral reconstructions are consistent with prior findings (Brancaccio et al., 2020) and demonstrate the accurate acquisition of sleep-wake states.

Long-range neural synchrony maps across sleep states

To evaluate the effect of sleep-wake state on local and long-range synchrony, we first performed a one-way ANOVA test assessing state as a factor. Within the delta frequency range, we identified statistically significant differences across sleep-wake states in local synchrony ($F = 1675.1$, $p \leq 0.0001$) and in long-range synchrony ($F = 164.9$, $p < 0.0001$). The global mean of local synchrony (i.e., relative spectral power averaged across all regions) monotonically increased from W to N1 and N2 (Fig. 2A). In contrast, the global mean of long-range synchrony increased from W to N1 (Fig. 2B; $t = 17.3$, $p < 0.001$, df = 1675) and W to N2 ($t = 13.5$, $p < 0.001$) and decreased from N1 to N2 ($t = -3.8$, $p < 0.001$) in the delta band. The relationship between mean regional local and long-range synchrony revealed no correlation within each sleep-wake state (Fig. 2C, purple, green, and red lines; W, $r = 0.219$, $p = 0.174$; N1, $r = 0.199$, $p = 0.220$; N2, $r = 0.159$, $p = 0.328$, respectively; Pearson's correlation). On the other hand, there was a high correlation across sleep-wake states between mean regional local and long-range synchrony (black line, $r = 0.839$, $p < 0.001$). These findings suggest that the spatial patterns of local synchrony do not strongly reflect that of long-range synchrony within classical stages of light NREM; however, regional local and long-range synchrony track across state changes. We next evaluated the spatial patterns of long-range synchrony across sleep-wake states. Mean imaginary coherence was computed for each region, revealing frequency-specific spatial patterns in wakefulness and light NREM (Figs. 2D, 3D, 4D,J,P). Within the delta band, long-range synchrony diffusely increased with highest connections within and across the bilateral frontal regions (i.e., superior frontal gyrus, middle frontal gyrus, precentral gyrus) and between the bilateral frontoparietal regions (i.e., between middle frontal gyrus, superior frontal gyrus and inferior parietal lobule, superior parietal lobule; Fig. 2E,F).

Within the theta frequency band, we again observed statistically significant differences across sleep-wake state in local synchrony ($F = 86.4$, $p < 0.0001$) and long-range synchrony ($F = 31.6$, $p < 0.0001$). Specifically, we observed the global mean of spectral power increased from W to N1 (Fig. 3A; $t = 11.8$, $p < 0.001$) and W to N2 ($t = 10.9$, $p < 0.001$); there was no statistical difference between N1 and N2 ($t = -1.0$, $p = 0.573$). The global mean of imaginary coherence was again observed to increase from W to N1 (Fig. 3B; $t = 6.1$, $p < 0.001$) and decrease from N1 to N2 ($t = -7.5$, $p < 0.001$) (i.e., as with the delta band), the peak long-range synchrony was in N1 within the theta band. The global mean of imaginary coherence was not statistically different
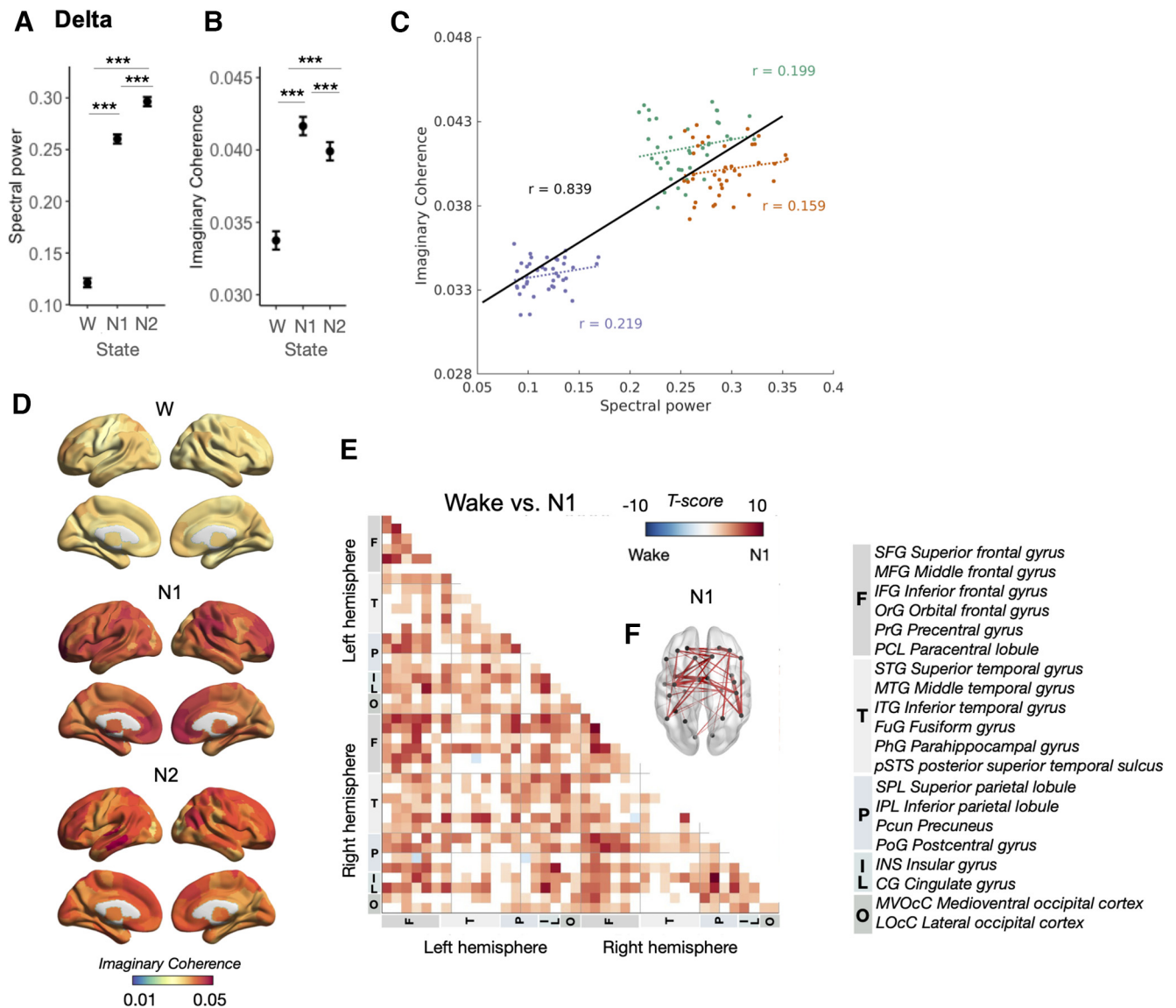
Figure 2. Spatial maps of long-range synchrony between sleep-wake states and the relationship between local and long-range synchrony in the delta frequency band. ***A***, Global mean of spectral power (local synchrony) for each sleep-wake state (W, N1, and N2) in the delta frequency band, as represented by LS-means and 95% CI. ***B***, Global mean of imaginary coherence (long-range synchrony) for each sleep-wake state, as represented by LS-means and 95% CI. ***C***, Association between mean regional long-range and local synchrony in the delta band. Each point represents an individual region within the spatial map. Linear regression and Pearson's correlations of the mean regional long-range and local synchrony measures are provided for within and across sleep-wake states. ***D***, Spatial maps of mean regional long-range synchrony, as measured by imaginary coherence, within the delta band across sleep-wake states. ***E***, T-score map of differences in long-range synchrony between W and N1 for region pairs within the delta band. Right-hand legend represents regions within each lobar segment, as represented on the *x* and *y* axes. ***F***, Top 50 highest positive functional connections, favoring N1.

between W and N2 ($t = -1.4$, $p = 0.333$). The relationship between mean regional local and long-range synchrony revealed a positive correlation within sleep-wake states (Fig. 3C, purple, green, and red; W, $r = 0.640$, $p < 0.001$; N1, $r = 0.407$, $p = 0.009$; N2, $r = 0.375$, $p = 0.017$, respectively), as well as when comparing across sleep-wake states ($r = 0.478$, $p < 0.001$). Furthermore, regional spatial maps revealed that the bilateral fronto-parieto-occipital regions (e.g., middle frontal gyrus, inferior frontal gyrus, medioventral occipital cortex, lateral occipital cortex, and precuneus) exhibited increased connectivity, while bilateral temporal regions revealed reduced intrahemispheric and interhemispheric connectivity (i.e., superior temporal gyrus, inferior temporal gyrus, middle temporal gyrus, hippocampus, and amygdala) in N1 compared with wake (Fig. 3D–F).

In addition, sleep-wake state effects were significant in both local and long-range synchrony measures in the alpha (Fig. 4A,B;

local: $F = 522.4$, $p < 0.0001$; long-range: $F = 40.2$, $p < 0.0001$), sigma (Fig. 4G,H; local: $F = 137.8$, $p < 0.0001$; long-range: $F = 98.1$, $p < 0.0001$), and beta (Fig. 4M,N; local: $F = 613.7$, $p < 0.0001$; long-range: $F = 36.1$, $p < 0.0001$) frequency bands. In the alpha frequency band, the correlation between mean regional local and long-range synchrony was strongest within the wake state (Fig. 4C; $r = 0.773$, $p < 0.001$), lower in N1 ($r = 0.608$, $p < 0.001$), and further reduced in N2 ($r = 0.428$, $p = 0.006$); the correlation remained strong across states ($r = 0.750$, $p < 0.001$). Furthermore, upon the transition from wakefulness to N1, the alpha band yielded an increase in long-range synchrony among interhemispheric fronto-temporal connections and a decrease within bilateral parieto-occipital regions (Fig. 4D–F). An asymmetry was also observed, characterized by an increase in long-range synchrony within the left frontal region and a diffuse decrease throughout the right hemisphere (Fig. 4E,F). Signifying
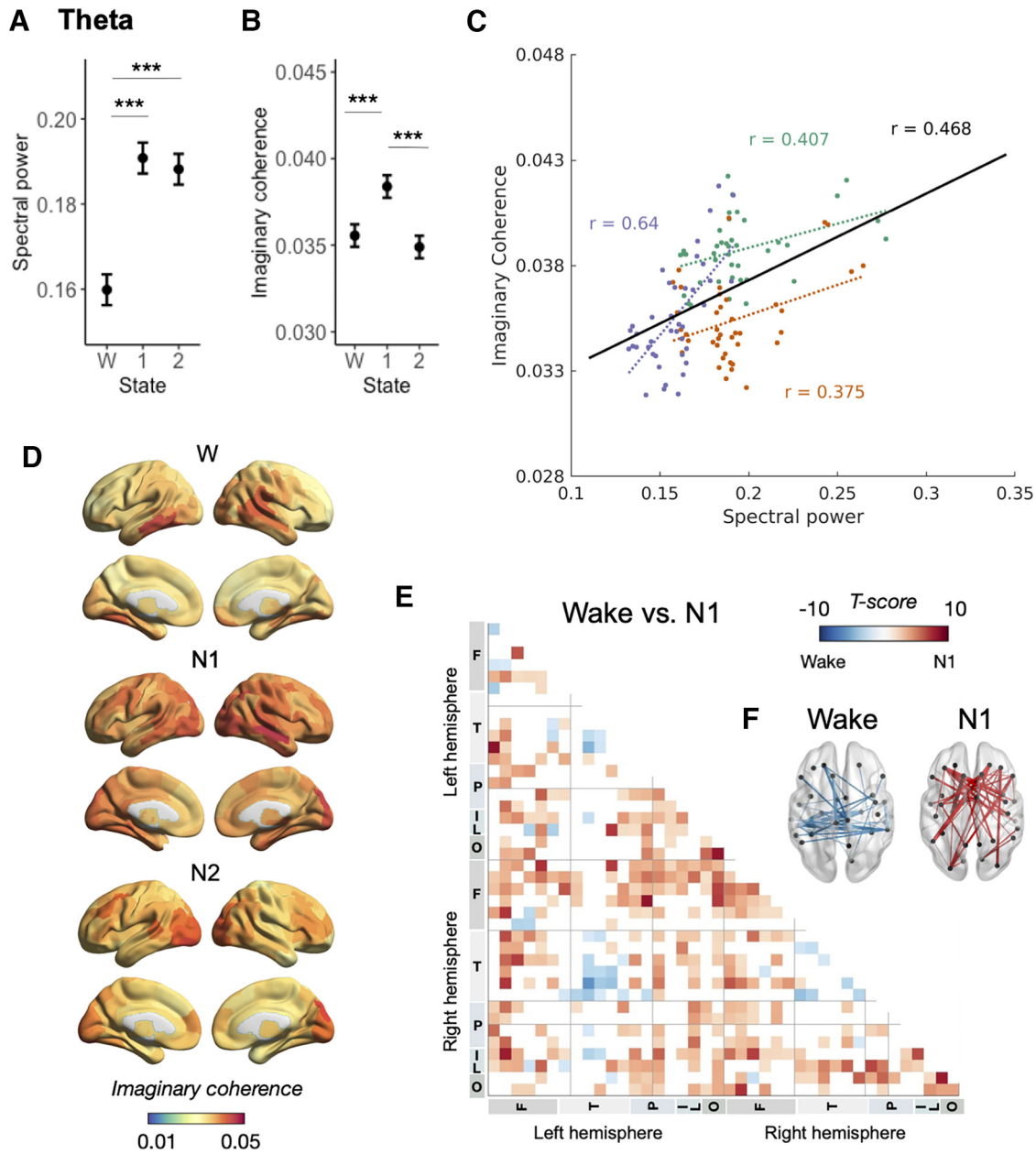
Figure 3. Spatial maps of mean long-range synchrony between sleep-wake states and the relationship between local and long-range synchrony in the theta frequency band. ***A***, Global mean of spectral power (local synchrony) for each sleep-wake state in the theta frequency band, as represented by LS-means and 95% CI. ***B***, Global mean of imaginary coherence (long-range synchrony) for each sleep-wake state, as represented by LS-means and 95% CI. ***C***, Association between mean regional local and long-range synchrony in the theta band. ***D***, Spatial maps of mean regional long-range synchrony in W, N1, and N2 within the theta band. ***E***, T-score map of differences in regional long-range synchrony between W and N1 within the theta band. ***F***, Top 50 highest positive and negative functional connections, favoring N1 (red) and W (blue), respectively.

the relevance of long-range versus local synchrony in the sigma band, long-range synchrony increased while local synchrony decreased upon transition from wakefulness to light NREM (Fig. 4G,H). As such, there was a negative correlation between the mean regional local and long-range synchrony across sleep-wake states (Fig. 4I; $r = -0.474$, $p < 0.001$), while there remained a positive correlation within W and N1 (W, $r = 0.406$, $p = 0.009$; N1, $r = 0.413$, $p = 0.008$) and no correlation in N2 ($r = 0.248$, $p = 0.123$). Spatial maps in the sigma band revealed a diffuse increase in connectivity from W to N1 with the strongest connections over the bilateral frontal regions (Fig. 4K,L). Within the beta band, a moderate positive correlation between the mean regional local and long-range synchrony was observed within the wake state (Fig. 4O; $r = 0.493$, $p = 0.001$), which was reduced in

N1 ($r = 0.351$, $p = 0.027$) and absent in N2 ($r = -0.044$, $p = 0.786$). In addition, the beta band demonstrated relatively increased synchrony in interhemispheric connectivity and anterior temporal regions in N1 compared with W (Fig. 4P–R). The frequency-specific activation patterns in N1 and N2 were similar; however, N1 overall demonstrated an increase in long-range neural synchrony compared with N2.

Directional information flow across sleep-wake states
Directional information flow, as measured by dPTE (Lobier et al., 2014; Kudo et al., 2021), provides insight into the regional inputs and outputs that may influence local activity and synchronization. Within the delta band, aggregated inflow targeting bilateral frontal regions increased in magnitude when
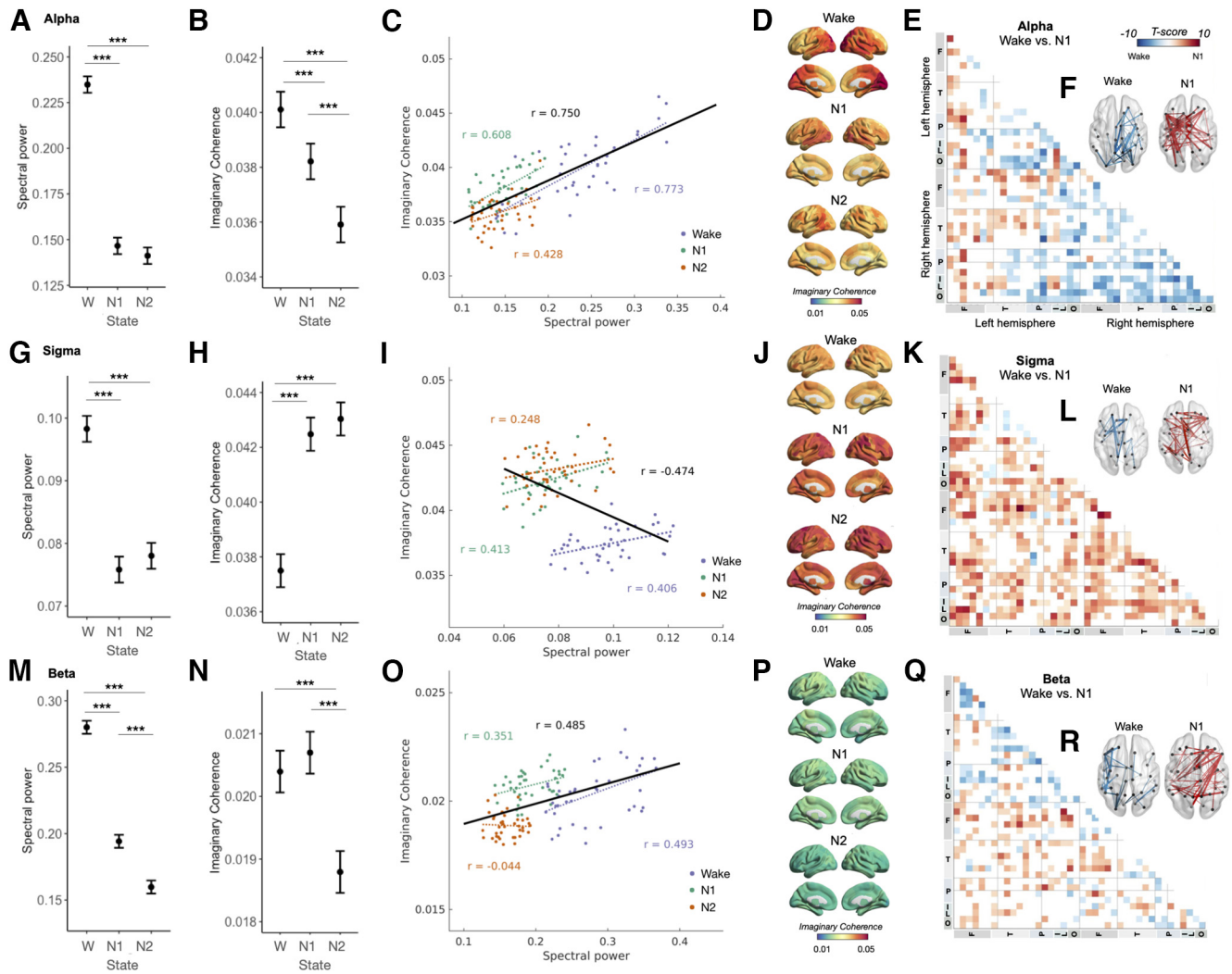
Figure 4. Spatial maps of mean long-range synchrony between sleep-wake states and the relationship between local and long-range synchrony in the alpha, sigma, and beta frequency bands. *A, G, M,* Global mean of spectral power (local synchrony) for each sleep-wake state in the alpha, sigma, and beta frequency bands, respectively, as represented by LS-means and 95% CI. *B, H, N,* Global mean of imaginary coherence (long-range synchrony) for each sleep-wake state, as represented by LS-means and 95% CI. *C, I, O,* Association between mean regional local and long-range synchrony in the alpha, sigma, and beta bands, respectively. *D, J, P,* Spatial maps of mean regional long-range synchrony in W, N1, and N2 within the alpha, sigma, and beta bands, respectively. *E, K, Q,* T-score map of differences in regional long-range synchrony between W and N1 within the alpha, sigma, and beta bands, respectively. *F, L, R,* Top 50 highest positive and negative functional connections, favoring N1 (red) and W (blue), within the alpha, sigma, and beta bands, respectively.

transitioning from W to N1 and from N1 to N2 (Fig. 5). Outflow from the bilateral occipital cortices (e.g., bilateral occipital polar cortex, lingual gyrus, inferior occipital gyrus, middle occipital gyrus, and ventromedial parieto-occipital sulcus) directly flowed to the orbital frontal cortices during wakefulness and more broadly to bilateral frontal regions and temporo-parietal regions during light NREM (Fig. 5B, C). With the transition from N1 to N2, the organization of information flow became more structured (Fig. 5B,C). Strikingly, as seen best in N2, the bilateral frontal regions were observed to receive inputs not only directly from the bilateral occipital regions, but also indirectly from the bilateral occipital regions via inputs to the bilateral temporal lobe, insula, and parietal regions (Fig. 5C,F,H). The serial flow of information, in which the bilateral frontal regions receive both direct and indirect inputs from broad cortical regions, reflects a hierarchical organization of information flow within the delta frequency band. Given the observed spatial patterns during light NREM, we speculate that the prominent anterior delta power seen at sleep onset may be

enabled through the inputs of broadly distributed and hierarchically organized cortical activity.

In the theta frequency band, we observed a reduction in temporo-occipital outflow to frontal regions and a relative increase in posterior temporo-parietal outflow to frontal regions with the transition from wakefulness to light NREM (Fig. 6A). In the alpha frequency band, there was an overall reduction in the occipital to frontal information flow, as well as a reduction of outflow from the precuneus and superior parietal lobule with the transition from wakefulness to light NREM (Fig. 6B). Within the sigma frequency band, there was a loss of outflow from insula-parieto-occipital regions to anterior temporal regions (Fig. 6C); whereas, in the beta frequency, there was also a reduction in outflow broadly from temporo-parieto-occipital regions to frontal regions (Fig. 6D). These findings suggest that with sleep onset, the posterior-anterior information flow most prominently observed in the alpha frequency band during wakefulness does not cease, but rather, shifts to lower frequencies during light NREM.
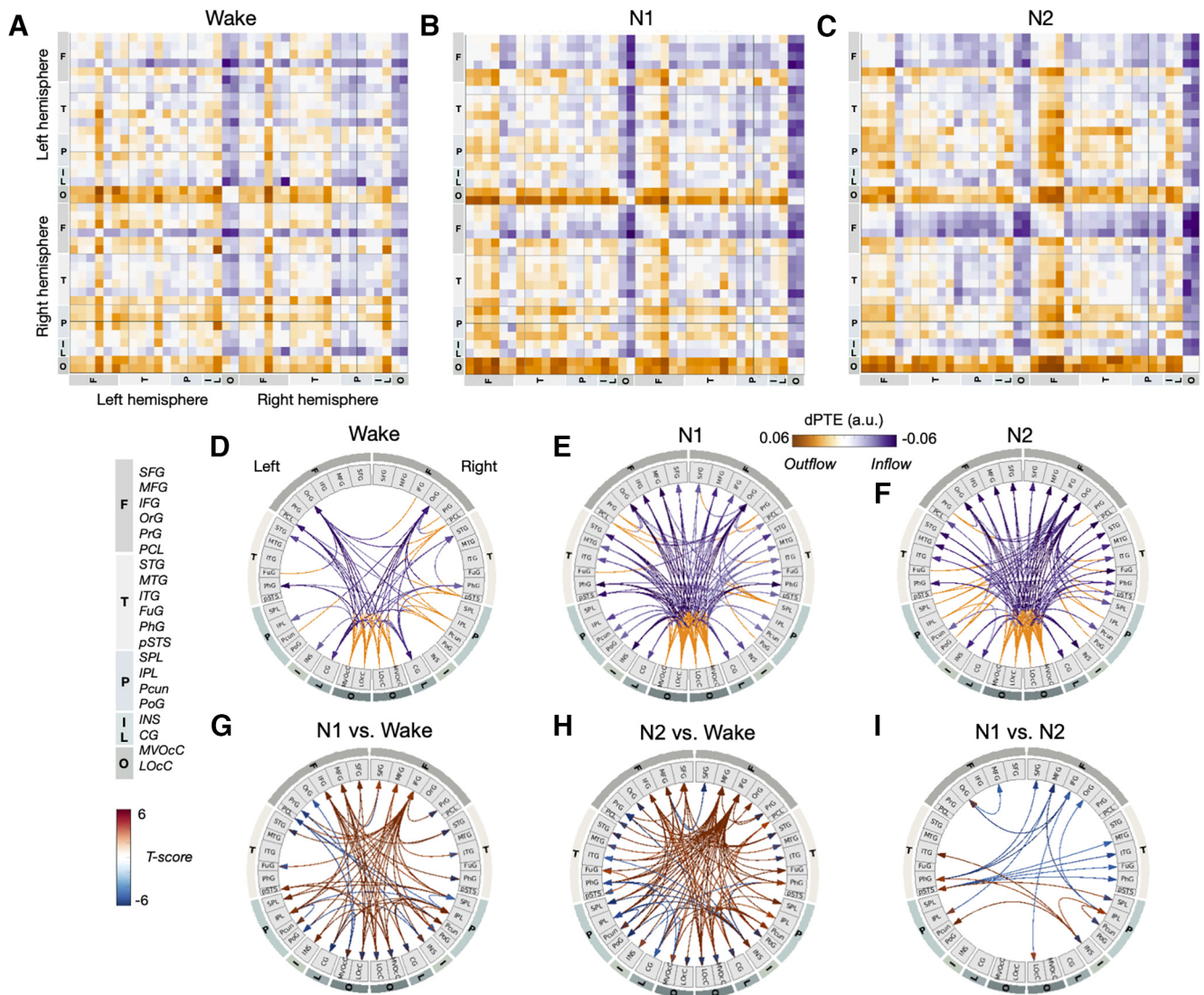
Figure 5. Directional information flow of sleep-wake states in the delta frequency band. ***A–C***, Directional information flow as measured by dPTE across W, N1, and N2. From W to N1 and N2, the bilateral frontal regions exhibited an increase in direct and indirect information flow. ***D–F***, Alternate visualization of directional information flow colored by orange (outflow) and purple arrow (inflow). The visualization represents the top 10% of information flow streams across sleep-wake states in the delta frequency. ***G–I***, Circle visualizations of *T* scores depicting the highest magnitude changes between specified states (accounting for FDR level 0.5 and *T*-score thresholding of 4).

Neural mass modeling of cortical excitation-to-inhibition parameters across sleep states

Finally, we utilized the observed physiology as inputs into biophysical NMMs to infer underlying mechanisms. Parameters of cortical excitation and inhibition were determined by modeling the observed regional spectral power using a deterministic NMM that captures local oscillatory dynamics (Fig. 7A). The two indices of the NMM that were optimized to fit local electrophysiology included the characteristic time constants (τ_e, τ_i), representing the time course of the underlying inhibitory and excitatory drive, and the gain (g_{ee}, g_{ii}), representing the strength of recurrent local circuits. From wakefulness to light NREM, both the g_{ee}/g_{ii} and the τ_e/τ_i ratio was observed to increase; differences between N1 to N2 were not statistically significant (Fig. 7B). The mean excitation-to-inhibition ratio (X_e/X_i), averaged across all regions, revealed an increase in excitation-to-inhibition from wake to light NREM (Fig. 7C; N1-W, $t = 4.3$, $p < 0.001$; N2-W, $t = 4.4$, $p < 0.001$); there was no significant difference between N1 and N2 ($t = -0.1$, $p = 0.99$). These findings suggest that the transitional period to sleep

may comprise a complex excitation-to-inhibition balance, in which local excitability-to-inhibition increases with the transition to light NREM.

By modeling local dynamics, the excitation-to-inhibition ratio was furthermore demonstrated to be spatially distinct across the cortical surface within sleep-wake states (Fig. 7D). The excitation-to-inhibition balance was highest over the bilateral frontal lobes during N1, while relatively reduced during wakefulness (Fig. 7E). Furthermore, the bilateral precuneus and posterior-cingulate exhibited relatively increased cortical excitation-to-inhibition during wakefulness, compared with light NREM (Fig. 7E). Comparison of the observed spectra to the model spectra (Fig. 7F) revealed an overall similarity in the profile of the spectra and peak frequencies. As homeostatic regulation during sleep has been thought to be achieved through tuning synaptic strengths to alter the excitation-to-inhibition balance (Tononi and Cirelli, 2006), our computational modeling suggests that the sleep transition may comprise of a spatially heterogeneous homeostatic cortical process.
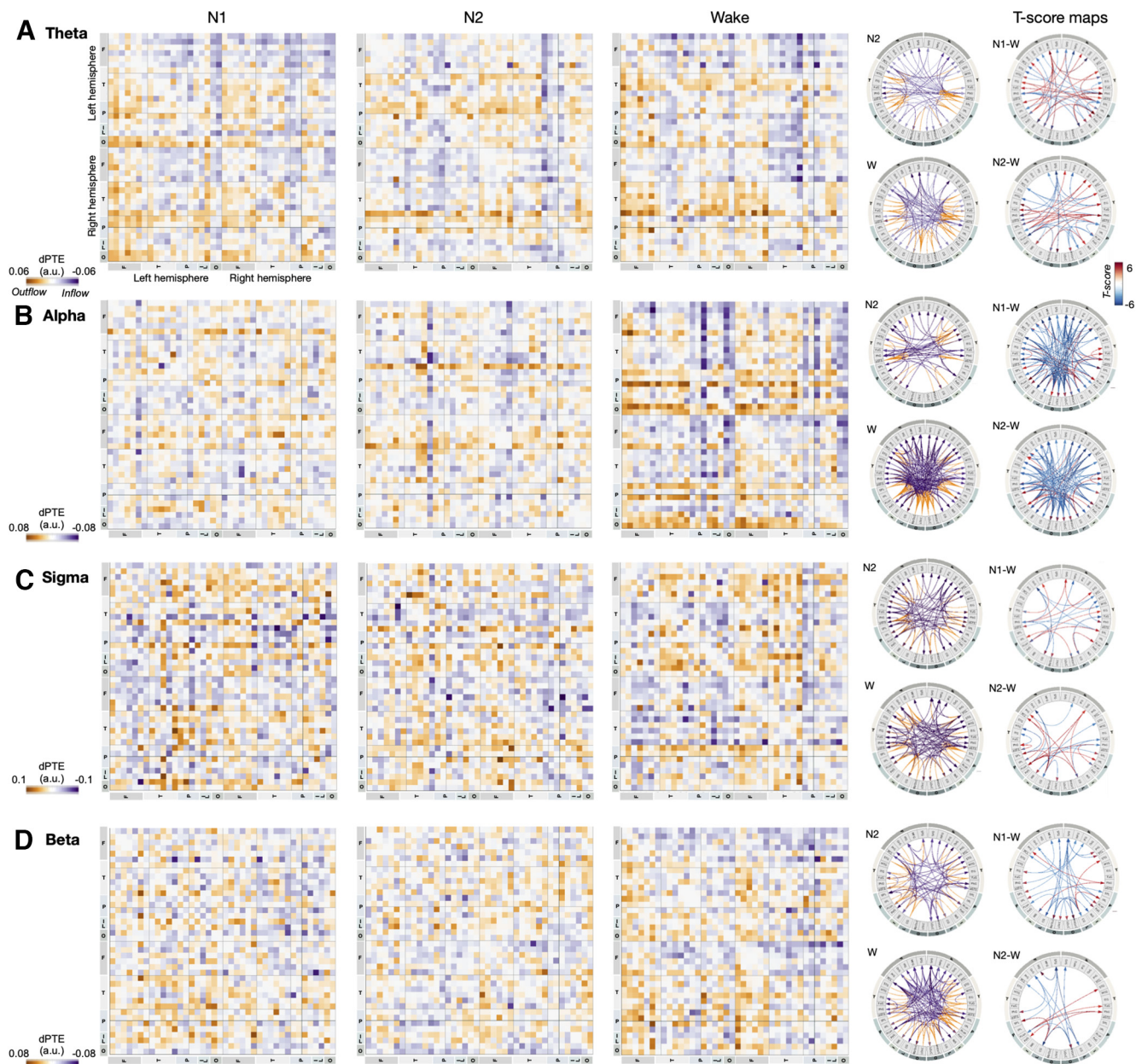
Figure 6. Directional information flow of sleep-wake states in the theta, alpha, sigma, and beta frequency bands. Directional information flow as measured by dPTE across W, N1, and N2 within the (**A**) theta, (**B**) alpha, (**C**) sigma, and (**D**) beta frequency bands. The color bar scales are adjusted for each frequency to enable comparison of spatial patterns and organization across sleep-wake states. Right-hand circle plots provide an alternate visualization of the top 10% of information flow streams for each frequency band computed across sleep-wake states; directional information flow is colored by orange (outflow) and purple arrow (inflow). The rightmost circle visualizations depict top T-score differences in directional information flow (thresholded by multiple comparison testing and T-score thresholding of 4).

Discussion

The characterization of whole-brain neural oscillations is essential to advancing our understanding of distributed network interactions underlying the transition to sleep. Descriptions of large-scale brain networks have relied chiefly on fMRI/PET imaging, which lack the temporal resolution and access to electrophysiology, and on EEG, which traditionally has limited spatial coverage and sensor-level analysis. By using MEG imaging, a whole-brain, high-density imaging methodology, to simultaneously evaluate spectral power, FC, and information flow, we identified local and long-range cortical structure that underlie the transition from waking to light NREM sleep. Our findings suggest that the transition from wakefulness to light NREM is accompanied by specific cortical patterns of neural synchrony that are coordinated

in frequency and spatial extent with relatively increased bilateral frontoparietal connections in the delta frequency band and decreased bilateral temporal and increased fronto-parieto-occipital connections in the theta band. Using directional measures of information flow, we furthermore identified a hierarchical flow of information to the bilateral frontal regions with sleep onset, characterized by both direct inputs from occipital regions and indirect inputs via the parieto-temporal regions. Finally, by using an NMM, we demonstrated spatially heterogeneous, anterior-posterior distribution of excitatory-to-inhibitory parameters upon the transition to sleep, potentially suggestive of local homeostatic processes. As a simultaneous evaluation of local and long-range synchrony and information flow has not yet been performed during sleep onset, we review the literature in
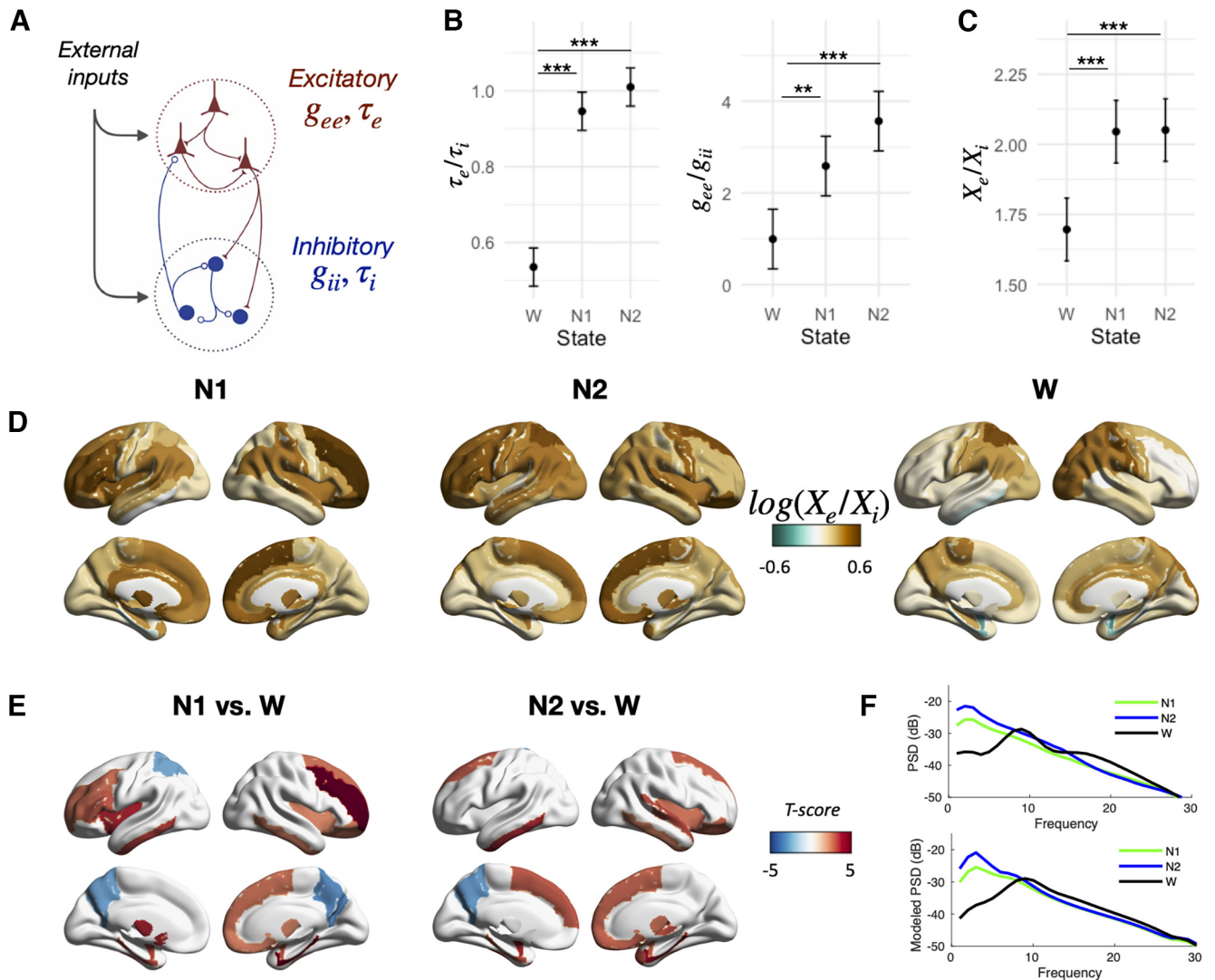
Figure 7. Biophysical NMM across sleep-wake states demonstrates spatially distinct excitation-to-inhibition patterns with the transition to sleep. **A**, Depiction of NMM, comprised of both excitatory and inhibitory inputs and modeled with time constants (τ) and gain (g) parameters. **B**, LS-means and 95% CI of global τ_e/τ_i and g_{ee}/g_{ii} parameters (i.e., computed across all regions and individuals as factors), comparing sleep-wake states. **C**, LS-means and 95% CI of global excitatory-to-inhibitory ratios (X_e/X_i) across sleep-wake states, revealing an increased excitation-to-inhibition with the transition from wake to light NREM. **D**, Spatial maps of mean regional $log(X_e/X_i)$ across sleep-wake states, revealing cortical heterogeneity in excitation-to-inhibition. **E**, Spatial maps of T scores reflecting changes in $log(X_e/X_i)$ between N1 versus W (left) and N2 versus W (right) at each anatomic region. Depicted T scores are thresholded across regions and sleep-wake state pairs to account for multiple comparison testing (FDR level 0.05). **F**, Actual (top) and modeled (bottom) PSD curves across sleep-wake states averaged across all regions.

each of these domains in the context of our findings and then elaborate on how our NMM modeling fits in with experimental techniques.

Studies from the past decade have revealed that sleep onset is not a homogeneous process (Werth et al., 1997; Marzano et al., 2013; Siclari et al., 2014; Bernardi et al., 2018; Fernandez Guerrero and Achermann, 2019). Seminal PET studies provided the initial evidence of differential deactivation of cortical association regions with the transition from wakefulness to NREM, including in the PFC, anterior cingulate, precuneus, and mesial temporal structures, in addition to the deactivation of subcortical structures (Braun et al., 1997; Maquet, 2000). Slow-wave activity using EEG/MEG has been identified to originate in anterior medial regions (Marzano et al., 2010; Siclari et al., 2014), later involving parietal, temporal, and occipital regions in an anterior to posterior direction (Siclari et al., 2014). The onset of slow-wave activity coincides with an early rise in delta power in the frontal regions (De Gennaro et al., 2001; Marzano et al., 2010; Ioannides et al., 2017) and an increase in theta synchrony in the

occipital region (Marzano et al., 2010; Fernandez Guerrero and Achermann, 2019). These findings are similarly recapitulated in our data (Fig. 1B), in which prominent delta power is represented in the mesial frontal regions. Across all frequency groups, regional local and long-range synchrony were poorly correlated (e.g., Figs. 2F, 3F), suggesting that the degree of long-range connectivity has minimal bearing on the observed local synchrony, for a given state. Similar findings in resting state between relative power and mean phase locking index in specific bands have been previously identified (Hillebrand et al., 2012), reaffirming the need to simultaneously evaluate both local and long-range synchrony measures. In contrast, we did identify a strong correlation between regional local and long-range synchrony across sleep-wake states, suggesting that a global factor related to state-change impacts both local and long-range synchrony. A possible physiologic interpretation includes an increase in global mean spiking rates, elicited from subcortical inputs, leading to increases in both local and long-range synchrony (Chawla et al., 1999).

Large-scale FC studies using fMRI (Spoormaker et al., 2010, 2011; Tagliazucchi and Laufs, 2014) and MEG (Liu et al., 2010b) have demonstrated widespread increases in long-range synchrony from W to N1 and N1 to N2, and a subsequent decrease in long-range synchrony with the transition to N3 (Spoormaker et al., 2010; Tagliazucchi et al., 2012; Tagliazucchi and Laufs, 2014). The widespread synchronization has been associated with a decrease in global integration (Boly et al., 2012) and theorized to account for the loss of consciousness with the transition to sleep. While we also demonstrate an increase in mean long-range synchrony from W to light NREM in delta/theta bands, our findings further reveal distinct long-range interactions during light NREM, such as relatively increased bilateral frontoparietal interactions in the delta band (Fig. 2B,C) and relatively decreased bilateral temporal and increased fronto-parieto-occipital interactions in the theta band (Fig. 3B,C). These findings differ from prior MEG studies (Liu et al., 2010b), which revealed homogeneous increases in coherence, possibly due to limitations of sensorbased FC mappings. Compared with spectral power, the mean long-range synchrony of N1 in the delta/theta band was identified to be higher than both W and N2, consistent with prior literature (Liu et al., 2010b; Spoormaker et al., 2010; Tagliazucchi and Laufs, 2014; Nguyen et al., 2018). These findings suggest that N1 represents a unique state that is not a transitional or ill-defined state between wakefulness and sleep, which has previously been suggested due to the relatively low interrater reliability of identifying N1 based on transitional PSG features (Rosenberg and Van Hout, 2013). Rather, the distinctly elevated global mean of long-range synchrony speaks to the complexity of the N1 state, which has been characterized by unique behavioral observations, including sleep mentation, responsiveness to sensory stimuli, or lucid dreaming (Goupil and Bekinschtein, 2012; Siclari and Tononi, 2017). In addition, an intriguing finding in the expanded evaluation of higher-frequency bands was the increased connectivity in the sigma band with an associated decrease in relative spectral power, upon the transition from wakefulness to sleep. Specifically, the increase in connectivity in both N1 and N2 remains unclear and cannot be fully accounted for by synchronized spindle activity, which emerges in N2 (Andrade et al., 2011). Prior studies suggest that graph characteristics within the sigma band, such as characteristic path length, a proxy for connectivity, tracks across light and deep NREM (Ferri et al., 2008), suggesting increased statespecific, resting-state connectivity within this frequency band, not specifically reflective of spindle activity. Furthermore, another possible contribution may be any ambient auditory stimuli heard while in the subject is resting MEG scanner, which has been demonstrated to increase sigma activity in both N1 and N2 (Wislowska et al., 2022). To this end, there may be ecological considerations to the neural data of sleeping in the MEG scanner versus a naturalistic, home environment (Iber et al., 2004; Bunford et al., 2018).

Complementing the evaluation of local and long-range synchrony across regions, we also assessed the directionality of regional interactions, as measured by directional information flow. Dominant posterior to anterior patterns of information flow of alpha frequencies have previously been identified during resting state (Hillebrand et al., 2016). Our findings recapitulated the posterior-to-anterior patterns of information flow during resting state for higher frequencies, and newly demonstrate increased organization of information flow within the delta frequency upon the transition to sleep. Specifically, information flow within the delta frequency is composed of (1) a direct posterior-to-anterior

pattern (i.e., flow from parieto-occipital regions to frontal regions), and (2) an indirect pattern (i.e., flow from occipital regions to bilateral parieto-temporal regions, which then flow to the bilateral frontal lobes; Fig. 4C,F) with the transition to light NREM (Hillebrand et al., 2016; Adamantidis et al., 2019). In contrast to prior EEG-based studies revealing an inversion of directionality from occipital-to-frontal to frontal-to-occipital during sleep onset (De Gennaro et al., 2004, 2005; Vecchio et al., 2017), our findings suggest a spectral shift in the prominent organizational pattern, while maintaining the posterior-to-anterior information flow. In addition to the increased number of sensors for source reconstruction approaches, MEG provides a reference free methodology for computing information flow, thereby preventing the potential bias associated with referenced based methods, such as EEG.

Finally, we investigated whether the observed neural oscillatory patterns may give rise to spatially heterogeneous model parameters of cortical excitation-to-inhibition. While it remains a challenge to directly measure neurotransmitter concentrations in human subjects, various methods to approximate excitation and inhibition balance have been used during sleep, including transcranial magnetic stimulation (TMS)/EEG, MRS, intracranial EEG with evoked responses (Meisel et al., 2015), and computational modeling (Ly et al., 2016). Cortical excitability has been demonstrated to increase with time awake and sleep deprivation (Huber et al., 2013; Meisel et al., 2015; Ly et al., 2016) and decrease during sleep and the circadian cycle (Ly et al., 2016; Miyawaki and Diba, 2016), as measured by neuronal firing rates, synchronization, and propagation of TMS (Massimini et al., 2005; Ly et al., 2016). Our NMM modeling suggests that the transition from wakefulness to light NREM is accompanied by a global increase in local cortical excitation-to-inhibition activity, consistent with prior methods using TMS (Massimini et al., 2005). Specifically, prior TMS findings revealed an enhancement of early or local TMS-EEG responses during sleep, followed by a global attenuation reflecting an overall global breakdown in effective cortical connectivity (Massimini et al., 2005). The amplified early or local TMS-EEG response has been hypothesized to relate to an increased drive of postsynaptic excitatory neurons, synchronization of local cortical populations, or activation of thalamocortical circuits. These findings are further consistent with methods using MRS to measure GABA and glutamate/glutamine concentrations to infer the excitatory-to-inhibitory balance, which identified an increase in NREM and a decrease in REM with visual learning (Pereira and Lewis, 2020; Tamaki et al., 2020). Importantly, the sleep-wake states captured in this study are limited to light NREM. As such, it remains consistent and possible that the transition to sleep is accompanied by a transient increase in the excitatory-to-inhibitory balance (i.e., during light NREM), which then decreases in deeper stages of NREM. Specifically, other studies have identified a reduced excitatory-to-inhibitory balance in slow-wave sleep (Niethard et al., 2016), which together with REM would support the synaptic homeostasis hypothesis associated with a global reduction in excitation across the night (Meisel et al., 2015; Ly et al., 2016; Niethard et al., 2017). These findings in healthy individuals based on computational modeling may be further supportive of sleep-wake observational patterns of epileptiform activity in epilepsy patients, as a clinical biomarker of excitability, in which light NREM has the highest state of epileptiform interictal and ictal activity, particularly in frontotemporal seizure onset localizations compared with wakefulness

(Herman et al., 2001; Ng and Pavlova, 2013; Peter-Derex et al., 2020).

By using local NMM modeling and leveraging whole-brain local field potential, cortical spatial maps of excitation-to-inhibition parameters can be elucidated, in contrast to seeded processes, for example, TMS impulses (Massimini M et al., 2005; Ly et al., 2016; Cardone et al., 2021), MRS (Tamaki et al., 2020), or direct measurements of excitatory and inhibitory neurotransmitters (Bridi et al., 2020). As such, we demonstrate that the modeled ratio of excitation-to-inhibition across the cortex is nonuniform (Fig. 5D,E), exhibiting an anterior-to-posterior gradient with the highest excitation-to-inhibition over bilateral frontal lobes during light NREM. In contrast, the highest excitation-to-inhibition during wakefulness is within the parietal-occipital regions, as commensurate with prior modeling (Bruining et al., 2020). Our findings support the view that sleep is composed of spatially heterogeneous network dynamics, which may reflect complex homeostatic patterns across the cortex.

This work has limitations. Due to the noisy environment and time limitations of a recording session within the MEG scanner, the sleep quality in the healthy participants was at times fragmented. In addition, deep NREM was not obtained across all participants and thus not included in the analysis. To address the sleep fragmentation, shortened epochs of high-quality 15 s were utilized and concatenated together to formulate the most faithful representations of sleep-wake states. Future efforts may benefit from overnight or sleep-deprived recording sessions to obtain longer, continuous periods of sleep-wake states. This study also incorporates a modest sample size of 14 healthy participants, who are also older in age. Indeed, older individuals have been described to have more variable sleep compared with younger adults (Mander et al., 2017; Li et al., 2018), yet the findings reported here are statistically significant across the cohort studied. Furthermore, FC, as measured by fMRI and EEG, has been demonstrated to be variable across ages, including lower overall connectivity in N2 in older individuals compared with younger participants (Ujma et al., 2019; Bouchard et al., 2020, 2021). Thus, we acknowledge that these reported findings should be taken in the context of the older mean age. Given prior findings that also reveal strong similarities across age (Daneault et al., 2021), additional future studies are necessary to comprehensively study aging effects and are of significant future interest. In addition, a fundamental limitation of current human electrophysiology recordings is the lack of simultaneous recordings from both whole-coverage cortical areas and subcortical structures, including the thalamus. Thus, the contributions of subcortical structures to the observed cortical synchrony patterns remain an open question. Finally, although the linear NMM captures the frequency spectra directly through a closed form solution, a primary limitation of the NMM used in this study includes its inability to capture nonlinear complexities of the brain. In addition, by design, the current model is capable of capturing two peaks, situated at or below the beta frequency range; current limitations of our NMM modeling include the inability to incorporate additional higher-frequency peaks under biologically plausible parameter conditions (Verma et al., 2022). While NMM modeling remains an exciting area of ongoing research, with several prior efforts demonstrating meaningful associations of model parameters with TMS-EEG outputs (Chellappa et al., 2016), there remain open questions with ongoing efforts to refine the parameter space and establish the robustness of NMMs. Future efforts are required to validate these models for establishing the

biological accuracy of modeled excitatory-to-inhibitory parameters (Verma et al., 2022, 2023; Cooray et al., 2023).

In conclusion, our work identifies cortical oscillations structured across multiple spatial scales and hierarchically organized across time (e.g., frequency-specific interactions) with the transition from wakefulness to light NREM sleep. Serial information flow from broad cortical regions is directed to the mesial frontal regions in the delta frequency, which may contribute to the synchronization of local oscillations. Finally, our observed electrophysiology gives rise to spatially heterogeneous parameters of cortical excitation-to-inhibition with the transition to sleep. Together, our findings suggest that the transition to sleep is accompanied by distinct, whole-brain frequency and spatially specific neural patterns that underlie spatially heterogeneous excitatory and inhibitory activity.

References

Adamantidis AR, Herrera CG, Gent TC (2019) Oscillating circuitries in the sleeping brain. Nat Rev Neurosci 20:746–762.

Andrade KC, Spoormaker VI, Dresler M, Wehrle R, Holsboer F, Sämann PG, Czisch M (2011) Sleep spindles and hippocampal functional connectivity in human NREM sleep. J Neurosci 31:10331–10339.

Bernardi G, Siclari F, Handjaras G, Riedner BA, Tononi G (2018) Local and widespread slow waves in stable NREM sleep: evidence for distinct regulation mechanisms. Front Hum Neurosci 12:248.

Boly M, Perlbarg V, Marrelec G, Schabus M, Laureys S, Doyon J, Pélégrini-Issac M, Maquet P, Benali H (2012) Hierarchical clustering of brain activity during human nonrapid eye movement sleep. Proc Natl Acad Sci USA 109:5856–5861.

Bouchard M, Lina JM, Gaudreault PO, Dubé J, Gosselin N, Carrier J (2020) EEG connectivity across sleep cycles and age. Sleep 43:zsz236.

Bouchard M, Lina JM, Gaudreault PO, Lafreniret A, Duba J, Gosselin N, Carrier J (2021) Sleeping at the switch. Elife 10:e64337.

Brancaccio A, Tabarelli D, Bigica M, Baldauf D (2020) Cortical source localization of sleep-stage specific oscillatory activity. Sci Rep 10:1–15.

Braun AR, Balkin TJ, Wesensten NJ, Carson RE, Varga M, Baldwin P, Selbie S, Belenky G, Herscovitch P (1997) Regional cerebral blood flow throughout the sleep-wake cycle: an H215O PET study. Brain 120:1173–1197.

Bridi MC, Zong FJ, Min X, Luo N, Tran T, Qiu J, Severin D, Zhang XT, Wang G, Zhu ZJ, He KW, Kirkwood A (2020) Daily oscillation of the excitation-inhibition balance in visual cortical circuits. Neuron 105:621–629.e4.

Brown RE, Basheer R, McKenna JT, Strecker RE, McCarley RW (2012) Control of sleep and wakefulness. Physiol Rev 92:1087.

Bruining H, Hardstone R, Juarez-Martinez EL, Sprengers J, Avramiea AE, Simpraga S, Houtman SJ, Poil SS, Dallares E, Palva S, Oranje B, Matias Palva J, Mansvelder HD, Linkenkaer-Hansen K (2020) Measurement of excitation-inhibition ratio in autism spectrum disorder using critical brain dynamics. Sci Rep 10:9195.

Bunford N, Reicher V, Kis A, Pogány Á, Gombos F, Bódizs R, Gácsi M (2018) Differences in pre-sleep activity and sleep location are associated with variability in daytime/nighttime sleep electrophysiology in the domestic dog. Sci Rep 8:7109.

Buzsáki G, Watson BO (2012) Brain rhythms and neural syntax: implications for efficient coding of cognitive content and neuropsychiatric disease. Dialogues Clin Neurosci 14:345.

Buzsáki G, Anastassiou CA, Koch C (2012) The origin of extracellular fields and currents: EEG, ECoG, LFP and spikes. Nat Rev Neurosci 13:407–420.

Cai C, Xu J, Velmurugan J, Knowlton R, Sekihara K, Nagarajan SS, Kirsch H (2019) Evaluation of a dual signal subspace projection algorithm in magnetoencephalographic recordings from patients with intractable epilepsy and vagus nerve stimulators. Neuroimage 188:161–170.

Cardone P, Van Egroo M, Chylinski D, Narbutas J, Gaggioni G, Vandewalle G (2021) Increased cortical excitability but stable effective connectivity index during attentional lapses. Sleep 44:1–11.

Chawla D, Lumer ED, Friston KJ (1999) The relationship between synchronization among neuronal populations and their mean activity levels. Neural Comput 11:1389–1411.

Chellappa SL, Gaggioni G, Ly JQ, Papachilleos S, Borsu C, Brzozowski A, Rosanova M, Sarasso S, Luxen A, Middleton B, Archer SN, Dijk DJ, Massimini M, Maquet P, Phillips C, Moran RJ, Vandewalle G (2016) Circadian dynamics in measures of cortical excitation and inhibition balance. Sci Rep 6:33661.

Cooray GK, Rosch RE, Friston KJ (2023) Global dynamics of neural mass models. PLoS Comput Biol 19:e1010915.

Daneault V, Orban P, Martin N, Dansereau C, Godbout J, Pouliot P, Dickinson P, Gosselin N, Vandewalle G, Maquet P, Lina JM, Doyon J, Bellec P, Carrier J (2021) Cerebral functional networks during sleep in young and older individuals. Sci Rep 11:4905.

David O, Friston KJ (2003) A neural mass model for MEG/EEG: coupling and neuronal dynamics. Neuroimage 20:1743–1755.

De Gennaro L, Ferrara M, Curcio G, Cristiani R (2001) Antero-posterior EEG changes during the wakefulness-sleep transition. Clin Neurophysiol 112:1901–1911.

De Gennaro L, Vecchio F, Ferrara M, Curcio G, Rossini PM, Babiloni C (2004) Changes in fronto-posterior functional coupling at sleep onset in humans. J Sleep Res 13:209–217.

De Gennaro L, Vecchio F, Ferrara M, Curcio G, Rossini PM, Babiloni C (2005) Antero-posterior functional coupling at sleep onset: changes as a function of increased sleep pressure. Brain Res Bull 65:133–140.

Fan L, Li H, Zhuo J, Zhang Y, Wang J, Chen L, Yang Z, Chu C, Xie S, Laird AR, Fox PT, Eickhoff SB, Yu C, Jiang T (2016) The human brainnetome atlas: a new brain atlas based on connectional architecture. Cereb Cortex 26:3508–3526.

Fernandez Guerrero A, Achermann P (2019) Brain dynamics during the sleep onset transition: an EEG source localization study. Neurobiol Sleep Circadian Rhythm 6:24–34.

Ferri R, Rundo F, Bruni O, Terzano MG, Stam CJ (2008) The functional connectivity of different EEG bands moves towards small-world network organization during sleep. Clin Neurophysiol 119:2026–2036.

Goupil L, Bekinschtein TA (2012) Cognitive processing during the transition to sleep. Arch Ital Biol 150:140–154.

Guggisberg AG, Honma SM, Findlay AM, Dalal SS, Kirsch HE, Berger MS, Nagarajan SS (2008) Mapping functional connectivity in patients with brain lesions. Ann Neurol 63:193–203.

Herman ST, Walczak TS, Bazil CW (2001) Distribution of partial seizures during the sleep-wake cycle: differences by seizure onset site. Neurology 56:1453–1459.

Hillebrand A, Barnes GR, Bosboom JL, Berendse HW, Stam CJ (2012) Frequency-dependent functional connectivity within resting-state networks: an atlas-based MEG beamformer solution. Neuroimage 59:3909–3921.

Hillebrand A, Tewarie P, van Dellen E, Yu M, Carbo EW, Douw L, Gouw AA, van Straaten EC, Stam CJ (2016) Direction of information flow in large-scale resting-state networks is frequency-dependent. Proc Natl Acad Sci 113:3867–3872.

Hobson JA, Pace-Schott EF (2002) The cognitive neuroscience of sleep: neuronal systems, consciousness and learning. Nat Rev Neurosci 3:679–693.

Horovitz SG, Fukunaga M, De Zwart JA, Van Gelderen P, Fulton SC, Balkin TJ, Duyn JH (2008) Low frequency BOLD fluctuations during resting wakefulness and light sleep: a simultaneous EEG-fMRI study. Hum Brain Mapp 29:671–682.

Horovitz SG, Braun AR, Carr WS, Picchioni D, Balkin TJ, Fukunaga M, Duyn JH (2009) Decoupling of the brain's default mode network during deep sleep. Proc Natl Acad Sci USA 106:11376–11381.

Huber R, Ghilardi MF, Massimini M, Tononi G (2004) Local sleep and learning. Nature 430:78–81.

Huber R, Mäki H, Rosanova M, Casarotto S, Canali P, Casali A, Tononi G, Massimini M (2013) Human cortical excitability increases with time awake. Cereb Cortex 23:332–338.

Iber C, Redline S, Gilpin AM, Quan SF, Zhang L, Gottlieb DJ, Rapoport D, Resnick HE, Sanders M, Smith P (2004) Polysomnography performed in the unattended home versus the attended laboratory setting: Sleep Heart Health Study methodology. Sleep 27:536–540.

Ioannides AA, Liu L, Poghosyan V, Kostopoulos GK (2017) Using MEG to understand the progression of light sleep and the emergence and functional roles of spindles and K-complexes. Front Hum Neurosci 11:313.

Klinzing JG, Niethard N, Born J (2019) Mechanisms of systems memory consolidation during sleep. Nat Neurosci 22:1598–1610.

Kringelbach ML, Deco G (2020) Brain states and transitions: insights from computational neuroscience. Cell Rep 32:108128.

Krone LB, Yamagata T, Blanco-Duque C, Guillaumin MC, Kahn MC, van der Vinne V, McKillop LE, Tam SK, Peirson SN, Akerman CJ, Hoerder-Suabedissen A, Molnár Z, Vyazovskiy V (2021) A role for the cortex in sleep–wake regulation. Nat Neurosci 24:1210–1215.

Krueger JM, Tononi G (2012) Local use-dependent sleep; synthesis of the new paradigm. Curr Top Med Chem 11:2490–2492.

Kudo K, Morise H, Ranasinghe KG, Mizuiri D, Bhutada AS, Chen J, Findlay A, Kirsch HE, Nagarajan SS (2021) Magnetoencephalography imaging reveals abnormal information flow in temporal lobe epilepsy. Brain Connect 12:362–373.

Larson-Prior LJ, Zempel JM, Nolan TS, Prior FW, Snyder A, Raichle ME (2009) Cortical network functional connectivity in the descent to sleep. Proc Natl Acad Sci USA 106:4489–4494.

Li J, Vitiello MV, Gooneratne NS (2018) Sleep in normal aging. Sleep Med Clin 13:1–11.

Liu Z, Fukunaga M, de Zwart JA, Duyn JH (2010a) Large-scale spontaneous fluctuations and correlations in brain electrical activity observed with magnetoencephalography. Neuroimage 51:102–111.

Liu Z, Fukunaga M, de Zwart JA, Duyn JH (2010b) Large-scale spontaneous fluctuations and correlations in brain electrical activity observed with magnetoencephalography. Neuroimage 51:102–111.

Lobier M, Siebenhühner F, Palva S, Palva JM (2014) Phase transfer entropy: a novel phase-based measure for directed connectivity in networks coupled by oscillatory interactions. Neuroimage 85:853–872.

Lombardi F, Herrmann HJ, de Arcangelis L (2017) Balance of excitation and inhibition determines 1/f power spectrum in neuronal networks. Chaos 27:047402.

Ly JQ, Gaggioni G, Chellappa SL, Papachilleos S, Brzozowski A, Borsu C, Rosanova M, Sarasso S, Middleton B, Luxen A, Archer SN, Phillips C, Dijk DJ, Maquet P, Massimini M, Vandewalle G (2016) Circadian regulation of human cortical excitability. Nat Commun 7:11828.

Mander BA, Winer JR, Walker MP (2017) Sleep and human aging. Neuron 94:19–36.

Maquet P (2000) Functional neuroimaging of normal human sleep by positron emission tomography. J Sleep Res 9:207–231.

Marzano C, Ferrara M, Curcio G, De Gennaro L (2010) The effects of sleep deprivation in humans: topographical electroencephalogram changes in non-rapid eye movement (NREM) sleep versus REM sleep. J Sleep Res 19:260–268.

Marzano C, Moroni F, Gorgoni M, Nobili L, Ferrara M, De Gennaro L (2013) How we fall asleep: regional and temporal differences in electroencephalographic synchronization at sleep onset. Sleep Med 14:1112–1122.

Massimini M, Ferrarelli F, Huber R, Esser S, Singh H, Tononi G (2005) Breakdown of cortical effective connectivity during sleep. Science 309:2228–2232.

Meisel C, Schulze-Bonhage A, Freestone D, Cook MJ, Achermann P, Plenz D (2015) Intrinsic excitability measures track antiepileptic drug action and uncover increasing/decreasing excitability over the wake/sleep cycle. Proc Natl Acad Sci USA 112:14694–14699.

Miyawaki H, Diba K (2016) Regulation of hippocampal firing by network oscillations during sleep. Curr Biol 26:893–902.

Moran R, Pinotsis DA, Friston K (2013) Neural masses and fields in dynamic causal modelling. Front Comput Neurosci 7:57.

Ng M, Pavlova M (2013) Why are seizures rare in rapid eye movement sleep? Review of the frequency of seizures in different sleep stages. Epilepsy Res Treat 2013:1–10.

Nguyen T, Babawale O, Kim T, Jo HJ, Liu H, Kim JG (2018) Exploring brain functional connectivity in rest and sleep states: a fNIRS study. Sci Rep 8:16144.

Niethard N, Hasegawa M, Itokazu T, Oyanedel CN, Born J, Sato TR (2016) Sleep-stage-specific regulation of cortical excitation and inhibition. Curr Biol 26:2739–2749.

Niethard N, Burgalossi A, Born J (2017) Plasticity during sleep is linked to specific regulation of cortical circuit activity. Front Neural Circuits 11:65.

Nolte G (2003) The magnetic lead field theorem in the quasi-static approximation and its use for magnetoencephalography forward calculation in realistic volume conductors. Phys Med Biol 48:3637–3652.

Oostenveld R, Fries P, Maris E, Schoffelen JM (2011) FieldTrip: Open source software for advanced analysis of MEG, EEG, and invasive electrophysiological data. Comput Intell Neurosci 2011:156869.

Palmer CA, Alfano CA (2017) Sleep and emotion regulation: an organizing, integrative review. Sleep Med Rev 31:6–16.

Pereira SI, Lewis PA (2020) Sleeping through brain excitation and inhibition. Nat Neurosci 23:1037–1039.

Peter-Derex L, Klimes P, Latreille V, Bouhadoun S, Dubeau F, Frauscher B (2020) Sleep disruption in epilepsy: ictal and interictal epileptic activity matter. Ann Neurol 88:907–920.

Ranasinghe KG, Verma P, Cai C, Xie X, Kudo K, Gao X, Lerner H, Mizuiri D, Strom A, Iaccarino L, La Joie R, Miller BL, Gorno-Tempini ML, Rankin KP, Jagust WJ, Vossel K, Rabinovici GD, Raj A, Nagarajan SS (2022) Altered excitatory and inhibitory neuronal subpopulation parameters are distinctly associated with tau and amyloid in Alzheimer's disease. eLife 11:e77850.

Raj A, Cai C, Xie X, Palacios E, Owen J, Mukherjee P, Nagarajan S (2020) Spectral graph theory of brain oscillations. Hum Brain Mapp 41:2980–2998.

Rajagovindan R, Ding M (2008) Decomposing neural synchrony: toward an explanation for near-zero phase-lag in cortical oscillatory networks. PLoS One 3:e3649.

Rosenberg RS, Van Hout S (2013) The American Academy of Sleep Medicine inter-scorer reliability program: sleep stage scoring. J Clin Sleep Med 9:81–87.

Sanchez Bornot JM, Wong-Lin KF, Ahmad AL, Prasad G (2018) Robust EEG/MEG based functional connectivity with the envelope of the imaginary coherence: sensor space analysis. Brain Topogr 31:895–916.

Saper CB, Fuller PM (2017) Wake-sleep circuitry: an overview. Curr Opin Neurobiol 44:186.

Sekihara K, Nagarajan SS (2008) Adaptive spatial filters. In: Adaptive Spatial Filters for Electromagnetic Brain Imaging. Series in Biomedical Engineering. Heidelberg, Berlin:Springer.

Sekihara K, Nagarajan SS, Poeppel D, Marantz A (2004) Asymptotic SNR of scalar and vector minimum-variance beamformers for neuromagnetic source reconstruction. IEEE Trans Biomed Eng 51:1726–1734.

Siclari F, Bernardi G, Riedner BA, LaRocque JJ, Benca RM, Tononi G (2014) Two distinct synchronization processes in the transition to sleep: a high-density electroencephalographic study. Sleep 37:1621–1637.

Siclari F, Tononi G (2017) Local aspects of sleep and wakefulness. Curr Opin Neurobiol 44:222–227.

Spoormaker VI, Schröter MS, Gleiser PM, Andrade KC, Dresler M, Wehrle R, Sämann PG, Czisch M (2010) Development of a large-scale functional brain network during human non-rapid eye movement sleep. J Neurosci 30:11379–11387.

Spoormaker VI, Czisch M, Maquet P, Jäncke L (2011) Large-scale functional brain networks in human non-rapid eye movement sleep: insights from combined electroencephalographic/functional magnetic resonance imaging studies. Philos Trans R Soc A Math Phys Eng Sci 369:3708–3729.

Sukenik N, Vinogradov O, Weinreb E, Segal M, Levina A, Moses E (2021) Neuronal circuits overcome imbalance in excitation and inhibition by adjusting connection numbers. Proc Natl Acad Sci 118:e2018459118.

Tagliazucchi E, Laufs H (2014) Decoding wakefulness levels from typical fMRI resting-state data reveals reliable drifts between wakefulness and sleep. Neuron 82:695–708.

Tagliazucchi E, von Wegner F, Morzelewski A, Brodbeck V, Laufs H (2012) Dynamic BOLD functional connectivity in humans and its electrophysiological correlates. Front Hum Neurosci 6:339.

Tamaki M, Wang Z, Barnes-Diana T, Guo D, Berard AV, Walsh E, Watanabe T, Sasaki Y (2020) Complementary contributions of non-REM and REM sleep to visual learning. Nat Neurosci 23:1150–1156.

Thomas CW, Guillaumin MC, McKillop LE, Achermann P, Vyazovskiy VV. (2020) Global sleep homeostasis reflects temporally and spatially integrated local cortical neuronal activity. Elife 9:1–25.

Tononi G, Cirelli C (2006) Sleep function and synaptic homeostasis. Sleep Med Rev 10:49–62.

Ujma PP, Konrad BN, Simor P, Gombos F, Körmendi J, Steiger A, Dresler M, Bódizs R (2019) Sleep EEG functional connectivity varies with age and sex, but not general intelligence. Neurobiol Aging 78:87–97.

Vecchio F, Miraglia F, Gorgoni M, Ferrara M, Iberite F, Bramanti P, De Gennaro L, Rossini PM (2017) Cortical connectivity modulation during sleep onset: a study via graph theory on EEG data. Hum Brain Mapp 38:5456–5464.

Verma P, Nagarajan S, Raj A (2022) Spectral graph theory of brain oscillations: revisited and improved. Neuroimage 249:118919.

Verma P, Nagarajan S, Raj A (2023) Stability and dynamics of a spectral graph model of brain oscillations. Netw Neurosci 7:48–72.

Viriyopase A, Bojak I, Zeitler M, Gielen S (2012) When long-range zero-lag synchronization is feasible in cortical networks. Front Comput Neurosci 6:49.

Vyazovskiy VV, Olcese U, Lazimy YM, Faraguna U, Esser SK, Williams JC, Cirelli C, Tononi G (2009) Cortical firing and sleep homeostasis. Neuron 63:865–878.

Wales DJ, Doye JP (1997) Global optimization by basin-hopping and the lowest energy structures of Lennard-Jones clusters containing up to 110 atoms. J Phys Chem A 101:5111–5116.

Werth E, Achermann P, Borbély AA (1997) Fronto-occipital EEG power gradients in human sleep. J Sleep Res 6:102–112.

Wislowska M, Klimesch W, Jensen O, Blume C, Schabus M (2022) Sleep-specific processing of auditory stimuli is reflected by alpha and sigma oscillations. J Neurosci 42:4711–4724.

Xia M, Wang J, He Y (2013) BrainNet viewer: a network visualization tool for human brain connectomics. PLoS One 8:e68910.